Interannual and decadal changes in the sea-air CO_2 flux from atmospheric CO_2 inverse modeling

Prabir K. Patra, Shamil Maksyutov, and Misa Ishizawa
Frontier Research Center for Global Change/Japan Agency for Marine-Earth Science and Technology, Yokohama, Japan

Takakiyo Nakazawa[1]
Center for Atmospheric and Oceanic Studies, Tohoku University, Sendai, Japan

Taro Takahashi and Jinro Ukita
Lamont-Doherty Earth Observatory, Columbia University, Palisades, New York, USA

Received 14 March 2004; revised 15 July 2005; accepted 26 August 2005; published 15 November 2005.

[1] The atmosphere-land-ocean fluxes of CO_2 were derived for 64 partitioned areas of the globe (22 over the ocean and 42 over the land) using a time-dependent inverse (TDI) model for the period of January 1988 to December 2001. The model calculation partially follow the TransCom-3 protocol, and is constrained by atmospheric CO_2 concentration data from 87 stations and fully time-dependent atmospheric transport model simulations. The air-to-land and air-to-sea fluxes averaged over the 1990s are estimated at 1.15 ± 0.74 and 1.88 ± 0.53 Pg-C yr^{-1}, respectively. These estimates, however, remain uncertain owing to sampling biases arising from the sparse distribution of atmospheric CO_2 data, are compared with other estimates by various methods. The sensitivity analysis indicates that the differences in fluxes and flux variability caused by the choices of initial conditions for the TDI model are smaller compared to those due to the selection of measurement networks. Our model results capture interannual variations in global and regional CO_2 fluxes realistically. The estimated oceanic CO_2 flux anomalies appear to be closely related to prominent climate modes such as El Niño–Southern Oscillation (ENSO), the North Atlantic Oscillation (NAO), and the Pacific Decadal Oscillation (PDO). The results from the correlation analyses show that the oceanic CO_2 flux in the tropics is strongly influenced by the ENSO dynamical cycle, and that in the sub-polar regions by upwelling of sub-surface waters in the winter and plankton blooms in the spring.

Citation: Patra, P. K., S. Maksyutov, M. Ishizawa, T. Nakazawa, T. Takahashi, and J. Ukita (2005), Interannual and decadal changes in the sea-air CO_2 flux from atmospheric CO_2 inverse modeling, *Global Biogeochem. Cycles*, *19*, GB4013, doi:10.1029/2004GB002257.

1. Introduction

[2] The atmospheric CO_2 concentration has been increasing for the past several decades at a rate of about one half of that expected for all the fossil fuel CO_2 emissions into the atmosphere. Although the consensus is that the missing half is absorbed by the ocean and the terrestrial biosphere, the estimates for their respective uptake fluxes vary over a wide range. The time series observations for atmospheric concentrations of CO_2 and O_2 indicate that the terrestrial carbon sink for the 1990s ranged from 0.7 ± 0.8 to 1.26 ± 0.8 PgC yr^{-1}, and the net ocean uptake from 2.4 ± 0.7 to 1.9 ± 0.6 Pg-C yr^{-1} [*Plattner et al.*, 2002; *Keeling and Garcia*, 2002]. Other measurements of CO_2 and $^{13}C/^{12}C$ in air and ocean water samples indicate that the net air-to-sea CO_2 flux over 1990s was in the range of 1.5 to 2 Pg-C yr^{-1} [e.g., *Battle et al.*, 2000; *Takahashi et al.*, 2002; *McNeil et al.*, 2003; *Gloor et al.*, 2003]. Ocean general circulation models also give similar estimates [*Sarmiento et al.*, 2000]. However, large discrepancies still exist among the temporal and spatial changes in the uptake flux, particularly at the interannual timescale [e.g., *Keeling et al.*, 1995; *Francey et al.*, 1995; *Battle et al.*, 2000]. The other independent method for CO_2 flux estimation is the inversion of atmospheric CO_2 data using atmospheric 3-dimensional transport models. In an effort to evaluate the details of the surface CO_2 flux variability on a regional scale, near-surface level atmospheric CO_2 concentrations have been incorporated into model simulations [e.g., *Tans et al.*, 1990; *Keeling et al.*, 1995; *Francey et al.*, 1995; *Rayner et al.*, 1999; *Bousquet*

[1]Also at Frontier Research Center for Global Change/Japan Agency for Marine-Earth Science and Technology, Yokohama, Japan.

0886-6236/05/2004GB002257

et al., 2000; *Rödenbeck et al.*, 2003]. The purpose of this study is to estimate the sea-air CO_2 fluxes at a spatial resolution of sub-basin scales and to address the relationships between the sea-air CO_2 flux and prominent climate modes including ENSO, the PDO and the NAO.

2. Computational Methods and Data

2.1. Inversion Technique

[3] The present study uses a time-dependent Bayesian inverse model, which was originally developed by *Rayner et al.* [1999]. Figure 1 shows 64 partitioned areas, for example, 22 over the ocean and 42 over the land as the inverse model framework is modified for this study. For our model calculation, we adopt the TransCom-3 protocol for the distribution of monthly pulses of regional sources (basis functions), background fluxes from net ecosystem exchange, oceanic exchange, and two maps of annual fossil fuel emission (representing 1990 and 1995) [*Gurney et al.*, 2000]. The oceanic basis functions are spatially fixed within a region, and the effects of a seasonally varying ice-cover are taken into account for the high latitudes. The monthly mean ecosystem fluxes from the CASA (Carnegie Ames Stanford Approach) biogeochemical model are normalized for the neutral terrestrial biosphere background flux (e.g., no net biosphere-atmosphere flux annually). The seasonal cycle of the sea-to-air flux is assumed to be stationary over the analysis period (referred here to as "cyclostationary") and is based on the climatological mean conditions normalized to 1995. The fossil fuel emission trend has been taken from *Marland et al.* [2003]. For the periods before 1992 and after 1996, the 1990 and 1995 fossil fuel emission distributions were used, respectively, and linearly interpolated for the period between them. In the TDI model, the monthly fluxes (S) and associated covariance (C_S) are calculated as

$$S = S_0 + \left(G^T C_D^{-1} G + C_{S_0}^{-1}\right)^{-1} G^T C_D^{-1} (D - GS_0) \qquad (1)$$

$$C_S = \left(G^T C_D^{-1} G + C_{S_0}^{-1}\right)^{-1}, \qquad (2)$$

where the elements of C_D and C_{S0} consist of the variance-covariance of atmospheric data (D) and prior sources (S_0), respectively, and G represents the atmospheric transport. The off-diagonal elements of C_{S0} are set to zero in this study, assuming that the flux regions are uncorrelated to one another. The correction fluxes (the second term in equation (1)) are determined from the differences between the atmosphere data and transport model simulation of prior sources scaled by data uncertainty. The uncertainty in source estimation is given as a combination of the information added by the data and our confidence on a priori sources (equation (2)). Thus the values of C_S (referred to as predicted or a posteriori flux covariance) can be used in comparison with C_{S0} (referred to as initial or a priori flux covariance) to determine the level of constraint imposed by the observations on the estimated fluxes ($C_S < C_{S0}$). The uncertainty of regional flux estimation is defined as the square root of diagonal elements in the flux variance-covariance matrix, and TDI-model region aggregation is made using $C_{\mathrm{aggr}} = \sum_{i,j=1}^{n} Cij$, where n is the number of aggregated regions. Even though some regions do not have atmospheric observations, their fluxes are estimated as a combination of weighted basis function signals and mismatches between the atmospheric data and model simulations for the other regions (see equation (1)). This also maintains the global balance between surface CO_2 fluxes and the atmospheric CO_2 burden. The spread (1σ) in CO_2 flux variability is calculated from an ensemble of TDI model runs by varying the initial conditions.

2.2. Forward Transport Model

[4] The NIES/FRCGC global transport model [*Maksyutov and Inoue*, 2000] was used to simulate the monthly and yearly tracer pulse functions. The model has 15 levels in the sigma coordinates and $2.5° \times 2.5°$ horizontal resolution. The transport model was forced by the 6-hourly NCEP/NCAR reanalysis data for the period of 1985–2002 [*Kistler et al.*, 2001]. Hence the resulting transports are not cyclostationary, but fully time dependent (i.e., interannually varying). The monthly mean climatological planetary boundary layer (PBL) heights (from the Data Assimilation Office at NASA's Goddard Space Flight Center) were used in the transport model. The PBL parameterization accounts for the winter-time CO_2 build up within the continental PBL but ignores the diurnal and synoptic timescale variations in PBL heights. While the selection of model transport model may play a significant role in determining regional flux distributions, a recent study shows that the flux anomalies can be derived with a greater degree of confidence by 13 member models of TransCom (D. F. Baker et al., TransCom 3 inversion intercomparison: Impact of transport model errors on the interannual variability of regional CO_2 fluxes, 1988–2003, submitted to *Global Biogeochemical Cycles*, 2005) (hereinafter referred to as Baker et al., submitted manuscript, 2005). Thus we associate greater confidence to the regional flux anomalies discussed in this study.

2.3. Atmospheric Data Selection

[5] The atmospheric CO_2 data and their associated uncertainties are prepared from the GlobalView data set [*Globalview-CO2*, 2002]. All the data networks used in this study and time of real-data coverage at 87 stations during the period 1988–2001 are shown in the auxiliary materials[1] (Figures S1 and Figure S2, respectively). These data represent atmospheric CO_2 concentrations near the surfaces of the oceans and land, and in the free troposphere. We have selected 87 stations for this study, where the GlobalView records commonly have observations more than 50% real-data during 1988–2001. Multiple case studies using different groups of CO_2 data set and choice of source region size have been carried out. Of these results, we have selected the best case on the basis of observed CO_2 data coverage and the ability of the TDI model to match the CO_2 data as shown in the next section, and refer it to as the "control run." Listed in the auxiliary material Table S1 are the 87

[1]Auxiliary material is available at ftp://ftp.agu.org/apend/gb/2004GB002257.

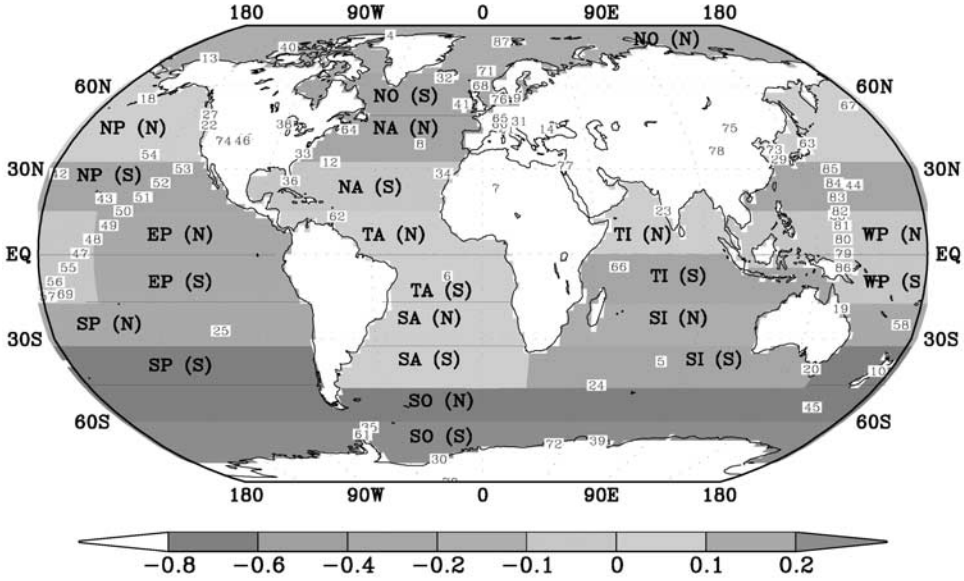

Figure 1. The 22 ocean regions in the TDI model (42 land regions, similar to those of *Patra et al.* [2005], are not shown here to avoid complexity) and the surface observation network (87 stations) used in this study. The long-term mean fluxes (except the 1997–1998 period) are indicated by the color of each region (see the color bar at the bottom of the figure). The negative and positive values indicate net uptake and net release by the ocean, respectively. Names of 11 ocean regions in TransCom-3 are as follows: 1, North Pacific (NP); 2, West Pacific (WP); 3, East Pacific (EP); 4, South Pacific (SP); 5, Northern Ocean (NP); 6, North Atlantic (NA); 7, Tropical Atlantic (TA); 8, South Atlantic (SA); 9, Southern Ocean (SO); 10, Tropical Indian (TI); and 11, South Indian (SI). These regions are divided into north (N) and south (S) parts in this work. Details of a priori and a posteriori flux uncertainties for the ocean regions are given in Table 2, and a glimpse of CO_2 concentrations and associated data uncertainties at each of the 87 stations are available in Table S1 in the auxiliary material. See color version of this figure at back of this issue.

stations used in this study and the annual CO_2 concentrations for the year 1999 and average data uncertainties estimated from the GlobalView data set. The differences between the observed and predicted concentrations by the inversion for the same time period are also shown. The "reference" data of GlobalView are used to fill the gaps in the "observed" records, and the average residual standard deviation (rsdav) have been used as the measure of data uncertainties following: $C_D = \sqrt{(0.3^2 + \text{rsdav}^2)}$. Thus the minimum data uncertainty is set at 0.3 ppm level. As a sensitivity test we have used the observation networks of varying sizes: 19 stations (Test-CR; as used by *Rödenbeck et al.* [2003]), 67 stations (Test-PB; as in the work by *Bousquet et al.* [2000]), 87 stations (Control Run; 76 stations of TransCom-3 plus 11 extra stations), and 100 GlobalView stations (Test-PP; 87 stations + 8 in South China Sea + 4 West Pacific Aircraft Sites + Ocean Station P, Canada).

2.4. Area Partition

[6] The inverse model is utilized to derive interannually varying fluxes from a large number of regions by the Bayesian approach, using an atmospheric CO_2 data network with a greater number of stations than in previous studies. The rationale behind increasing the number of area partitions in the inverse model is to reduce regional aggregation error, and to obtain extra information on spatial and temporal CO_2 variability for CO_2 data and sources. To understand the effect of increasing source regions on fitting CO_2 data and sources, we defined χ^2 as

$$\chi^2 = {}^1\!/_T \left[\frac{1}{N} \sum_1^N \left[\left(D - D_{predicted}\right)^2 / C_D + \frac{1}{M} \sum_1^M (S_0 - S)^2 / C_S \right] \right],$$

where, T, N and M are number of time intervals, observation stations and source regions, respectively, $D_{Predicted}$ is a posteriori CO_2 data or G•S. By increasing the number of regions from 22 to 64, value of χ^2 is reduced from 2.15 to 1.11. This suggests that the assumption of 100% correlation within one large region tends to obscure some of the information available in the observations. The value of χ^2 is further reduced to 0.99 when the interannually varying meteorological fields are utilized instead of the 1997 meteorological fields (dropping the cyclostationary assumption). This result indicates that the east-west and north-south gradients in CO_2 observations are fitted better by the transport model simulations using real-time meteorological fields. On the

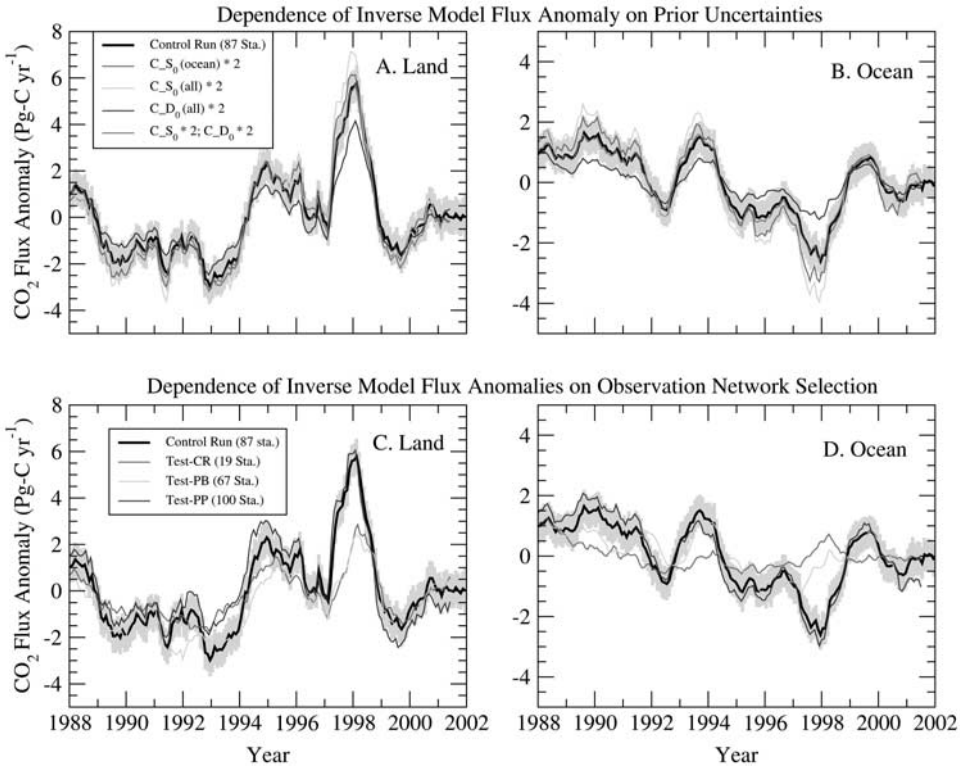

Figure 2. Six-monthly running averages of CO_2 flux anomalies as estimated by TDI calculation for total land and ocean from atmospheric CO_2 data, with varying network sizes as well as different a priori data and source uncertainties. Flux anomaly is calculated by subtracting an average seasonal cycle for the period 1988–2001 from the monthly-mean CO_2 fluxes. The cases shown in Figures 2a and 2b are obtained by (1) control run (thick black line), (2) ocean $C_{S0} \times 2$, (3) all $C_{S0} \times 2$, (4) $C_D \times 2$, and (5) all $C_{S0} \times 2$ and $C_D \times 2$. The cases shown in Figures 2c and 2d are obtained by (1) control run, and different CO_2 data networks, (2) Test-CR, (3) Test-PB, and (4) Test-PP. The a posteriori flux estimate uncertainties obtained from control TDI model run are shown as the grey shading. The tick marks indicate January of the corresponding years. See color version of this figure at back of this issue.

other hand, when the number of partitioned areas is increased, atmospheric observations would become unavailable for some areas to constrain the fluxes. Accordingly, too many partitions would risk generating unrealistic flux behaviors and driving up the error in flux estimation.

3. Results and Discussion

3.1. Global Fluxes and Land-Ocean Partitioning

[7] Net CO_2 flux to the atmosphere for the global land ecosystems, averaged over 1990–2000, is estimated about -1.15 Pg-C yr^{-1} with the range of $-1.05 \sim -1.40$ Pg-C yr^{-1} and a posteriori uncertainty of ≈ 0.74 Pg-C yr^{-1}; and that for the global ocean is -1.88 Pg-C yr^{-1} with the range of $-1.58 \sim -2.02$ Pg-C yr^{-1} and a posteriori uncertainty of ≈ 0.53 Pg-C yr^{-1}. Note that the 1997/1998 El Niño period was excluded since the CO_2 flux anomalies were extreme in the whole period of our analysis as will be discussed later. The ranges in both fluxes have been estimated on the basis of five sensitivity runs by varying the initial conditions for inverse simulations as defined in Figures 2a and 2b. Comparing our estimates to others (Table 1), we find that these values are within the range of some previous estimates that are based on various independent approaches [e.g., *Plattner et al.*, 2002; *Takahashi et al.*, 2002]. On the other hand, compared to our results, typically greater uptakes by lands and lesser uptakes by the oceans have been obtained by several inverse model studies [*Bousquet et al.*, 2000; *Rödenbeck et al.*, 2003; *Gurney et al.*, 2004; Baker et al., submitted manuscript, 2005], and other independent estimates after correcting for the riverine fluxes (see Table 1) [*Prentice et al.*, 2001; *Keeling and Garcia*, 2002]. The differences between inverse model results appear to arise mainly from the inverse model frameworks, the selection of measurement networks and the periods of inversion (mainly with or without the 1997/1998 El Niño period; see Table 1). The atmospheric CO_2 concentrations over the land areas generally have larger variability compared to the ocean regions because of the local weather conditions and the presence of small-scale strong local sinks/sources. As a result, the estimated interannual variability is larger for the

Table 1. Comparison of Different Estimates of Global Land and Ocean to Atmosphere CO_2 Fluxes in the Period 1990–2000[a]

Averaging Period	This Work		Other Estimates		
	Land	Ocean	References	Land	Ocean
		Estimate Without 1997/1998 Period			
1990–1996, 1999–2000	1.15 (±0.7)	1.88 (±0.5)	TT03		1.46–2.12
		Estimates Using Atmospheric O_2/N_2[b]			
1990–2000	0.45	2.22	KG02	1.26 ± 0.8	1.86 ± 0.6
1990–1999	0.41	2.21	GKP02	0.70 ± 0.8	2.40 ± 0.7
1990–1999			IPCC	1.40 ± 0.7	1.70 ± 0.5
		Estimates Using Inverse Modeling of Atmospheric CO_2			
1990–1999			CR03	1.60 ± 0.3	1.70 ± 0.2
1992–1997	0.57	2.21	PB00	1.40 ± 0.8	1.80 ± 0.6
1992–1996	0.63	2.25	KRG04	1.46 ± 0.6	1.34 ± 0.6
1991–2000	0.31	2.35	DFB05	2.09 ± 0.5	1.06 ± 0.5

[a]Units are Pg-C yr^{-1}. References: TT03, *Takahashi et al.* [2002] (updated value, corresponds to year 1995); KG02, *Keeling and Garcia* [2002]; GKP02, *Plattner et al.* [2002]; IPCC, *Prentice et al.* [2001]; CR03, *Rödenbeck et al.* [2003]; PB00, *Bousquet et al.* [2000]; KRG04, *Gurney et al.* [2004]; DFB05, Baker et al. (submitted manuscript, 2005).

[b]These estimates account for land-ocean carbon transport through the rivers. For comparison with inverse model results, 0.6 Pg-C yr^{-1} [*Aumont et al.*, 2001] may be added to and subtracted from the land and ocean fluxes, respectively.

land uptake ~1.92 Pg-C yr^{-1} (1σ) (ranging from +3.06 to −2.63 Pg-C yr^{-1}) and relatively small for ocean uptake ~1.08 Pg-C yr^{-1} (ranging from −0.68 to −4.19 Pg-C yr^{-1}) during the period 1990–2000 (in control run case only).

3.2. Ocean Region Fluxes

[8] The 1988–2001 mean fluxes computed for each of the 22 ocean regions are summarized in Table 2. They are compared with the climatological mean sea-air fluxes estimated by T. Takahashi and coworkers for non-El Niño conditions [*Takahashi et al.*, 2003] (hereinafter referred to as TT03, also available at www.ldeo.columbia.edu/CO2) on the basis of the observed sea-air pCO_2 difference over the global oceans. The TT03 climatology of oceanic flux distribution (normalized to a reference year of 1995) is an updated version of the background ocean flux [*Takahashi et al.*, 2002] using about 1.5 million pCO_2 measurements, and NCEP 41-year mean wind speeds at 10 m above sea surface. Thus TT03 can be treated as an independent estimate from the prior ocean flux. Our results show that the Northern Ocean (NO), North Atlantic (NA), southern North Pacific (NP(S)), South Indian (SI) and northern Southern Ocean (SO(N)) are net sinks of CO_2 during all years, whereas the Eastern Pacific (EP) is a net source for the atmosphere. In general, our results are consistent with TT03 (see Figure 1 for the abbreviations).

[9] However, significant differences are observed in the following areas (Table 2). In the northern North Pacific (NP(N)), our model yields a weak source of 0.03 Pg-C yr^{-1},

Table 2. Comparison of CO_2 Fluxes From 22 Ocean Regions, Averaged Over the Period 1988–2001, With the TT03 Fluxes[a]

Region Name	Prior		Predicted		TT03	
	Flux	Uncertainty	Flux	Uncertainty	WM99	W92
NP(S)	−0.13	1.16	−0.32	0.55	−0.22	−0.24
NP(N)	−0.36	1.16	0.03	0.63	−0.26	−0.33
WP(S)	0.06	0.71	−0.02	0.42	0.02	0.01
WP(N)	0.08	0.71	−0.07	0.48	0.07	0.05
EP(S)	0.29	0.79	0.16	0.65	0.41	0.37
EP(N)	0.17	0.79	0.17	0.37	0.16	0.12
SP(S)	−0.17	1.72	−0.66	1.04	−0.17	−0.19
SP(N)	−0.05	1.72	0.10	0.69	−0.08	−0.08
NO(S)	−0.24	0.37	−0.27	0.31	−0.20	−0.25
NO(N)	−0.18	0.37	−0.10	0.31	−0.08	−0.10
NA(S)	−0.03	0.56	−0.07	0.45	−0.06	−0.06
NA(N)	−0.25	0.56	−0.21	0.46	−0.21	−0.26
TA(S)	0.10	0.56	0.09	0.48	0.13	0.11
TA(N)	0.02	0.56	0.05	0.49	0.03	0.02
SA(S)	−0.18	0.68	0.00	0.61	−0.16	−0.19
SA(N)	0.06	0.68	0.07	0.60	0.04	0.03
SO(S)	−0.14	2.12	0.32	0.49	−0.03	−0.03
SO(N)	−0.73	2.12	−0.67	1.21	−0.51	−0.69
TI(S)	0.03	1.05	−0.22	0.78	0.03	0.01
TI(N)	0.08	1.05	0.05	0.91	0.13	0.14
SI(S)	−0.36	0.76	−0.29	0.44	−0.31	−0.40
SI(N)	−0.19	0.76	−0.13	0.71	−0.16	−0.15

[a]Units are Pg-C yr^{-1}. Two sets of *Takahashi et al.* [2002] (TT03) fluxes were obtained using 41-year mean NCEP wind speeds and two formulations for the wind speed dependence on the air-sea CO_2 gas transfer coefficient, W92 [*Wanninkhof*, 1992] and WM99 [*Wanninkhof and McGillis*, 1999].

whereas TT03 gives a strong sink of −0.26 Pg-C yr^{-1}. In the tropical eastern Pacific (EP(S)), our model gives a source flux of 0.16 Pg-C yr^{-1}, which is about 30% of the TT03 value of 0.41 Pg-C yr^{-1}. Our study also gives a strong source of 0.32 Pg-C yr^{-1} for the high-latitude Southern Ocean (SO(S)), whereas TT03 gives a weak sink of −0.03 Pg-C yr^{-1}. Tropical Indian Ocean (TI(S)) is a strong sink of −0.22 Pg-C yr^{-1} by our study, whereas it is a very weak source of 0.03 Pg-C yr^{-1} by TT03. These areas, where significant discrepancies are observed between TT03 and our atmospheric CO_2 inverse study, have no observations or are lacking in representative observations as shown in Figure 1. Hence our flux values are not strongly constrained. Furthermore, according to our study, the southern South Pacific (SP(S)) is a very strong CO_2 sink of −0.66 Pg-C yr^{-1}, whereas TT03 gives a moderate sink of −0.17 Pg-C yr^{-1}.

3.3. Sensitivity Tests for Interannual Variability (IAV)

[10] In order to evaluate the impact of different compositions of the CO_2 network, the size of the network is changed from 19 stations up to 100 stations (Test-PP), and dependence of estimated fluxes on the a priori flux and atmospheric data uncertainties is examined. Figure 2 shows the estimated flux anomalies for the aggregated global land and ocean regions. Though the net fluxes from individual regions vary, the estimated anomalies are quite stable against the selection of inputs to the inverse model (Figures 2a and 2b). When the CO_2 data uncertainties are doubled in the 87-station control run, the interannual flux variability is reduced significantly. This suggests that the inverse model results depend primarily on the CO_2 observations and less on the model initialization itself. To confirm this further, we have tried to mimic the results of previous investigators using our model but selecting similar stations which were used in their studies (Test-PB using 67 stations and Test-CR using 19 stations; see Figures 2c and 2d). The land fluxes are broadly reproduced by Test-CR, Test-PB, and the control run, except that the control run yields a larger emission from the land during 1997–1998 period. The carbon source anomalies from the global land for the 1997 and 1998 are estimated at 3.48 and 2.65 Pg-C yr^{-1}, respectively (control run). Detailed discussion on interannual and regional CO_2 flux variability can be found elsewhere [*Patra et al.*, 2005].

[11] The variability in ocean fluxes that is obtained using smaller size observation networks (i.e. Test-CR (19 stations) and Test-PB (67 stations)) is considerably smaller than those derived using the 87-station network. On the other hand, Test-PP (100 stations) produces a similar flux variability as that in the control run (Figure 2d). Because the additional stations have smaller number of CO_2 observations compared to the observation network used in the control run, they do not seem to significantly affect the inverse model results. In addition, the uncertainties assigned to CO_2 data over the South China Sea (eight stations) are relatively large (∼1.0 ppm) compared with those for western Pacific Ocean aircraft observations (∼0.5 ppm). These results indicate that the model flux is sensitive to the selection of the atmospheric CO_2 data.

3.4. IAV: Comparison With Other Estimations

[12] The variability in global sea-air CO_2 fluxes obtained from five atmospheric CO_2 inverse model studies and one ocean GCM study are compared with the results of this study for the period of 1988–2001 (Figure 3). The estimated flux anomalies obtained by various groups using different modeling approaches differ greatly from each other. As already discussed in section 3.3 and shown in the auxiliary materials, the disagreement between the model results are attributable primarily to the selection of observational networks. Of these model studies, the results of two studies show positive CO_2 flux anomalies during the intense 1997/1998 El Niño period, whereas three, including our results, show negative anomalies and two show almost no effect. Our results are broadly consistent with those of *Keeling et al.* [2001], especially in the period after 1990, and with more recent results by Baker et al. (submitted manuscript, 2005). Therefore we will discuss mainly the results of these three models below.

[13] During the strong 1997/1998 El Niño period, these results indicate a significant increase in the global ocean uptake, i.e., negative anomalies. Our TDI model suggests an increase in CO_2 uptake by ∼1.3 Pg-C yr^{-1} compared to previous 3 years. Since one of the most pronounced effects of an El Niño event is a reduction of the sea-to-air CO_2 flux due to the suppression of upwelling high-pCO_2 waters in the eastern equatorial Pacific, it accounts for a negative flux anomaly or an increase in the ocean CO_2 uptake. However, the magnitude of anomalies obtained by this study is as large as −2.7 Pg-C yr^{-1} and that exceeds the mean equatorial Pacific flux of ∼1 Pg-C yr^{-1} estimated for the non-El Niño periods on the basis of the sea-air pCO_2 difference observations [*Feely et al.*, 1999; *Takahashi et al.*, 2002]. Hence, if our results are taken literally, an intensification of oceanic sink areas outside the equatorial Pacific is implied during the 1997/1998 El Niño period.

[14] An increase in the oceanic uptake of atmospheric CO_2 during the 1991/1992 El Niño event was proposed by *Francey et al.* [1995] on the basis of the $\delta^{13}C$ changes in the atmospheric CO_2. Our results as well as those of *Keeling et al.* [2001] and Baker et al. (submitted manuscript, 2005) also show an increase in ocean uptake (or negative anomalies) for the 1991/1992 El Niño event as well as the weak 1994/1995 event. However, all these studies exhibit positive anomalies during the weak 1992/1993 El Niño. The results obtained using an ocean GCM tend to produce a negative ocean flux anomalies during the 1991/1992, 1992/1993 and 1997/1998 El Niño periods [*Le Quéré et al.*, 2003], but their anomalies are much smaller than those predicted by the inverse models.

3.5. IAV: Comparison With Ocean Observations

[15] We compare our results with the time series observations made in three oceanic areas. In Figure 4a, the flux changes in the equatorial Pacific region are shown. Our results are in good agreement with the direct estimations based on surface water pCO_2 measurements by *Feely et al.*

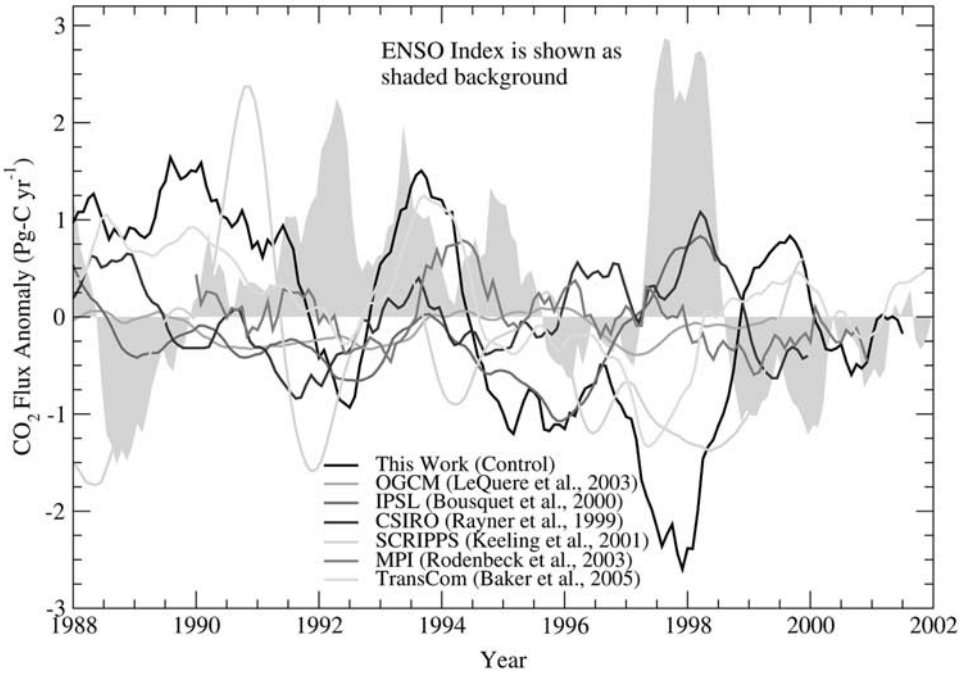

Figure 3. Global ocean flux anomalies (deseasonalized) estimated by different groups using inverse models, ocean models, and carbon isotope deconvolution techniques. The description of OGCM, CSIRO, and SCRIPPS models can be found in details elsewhere [*Le Quéré et al.*, 2003, and references therein]. The results from *Rödenbeck et al.* [2003] are due to an observation network of 19 stations, which is selected to show the flux variability for the 1990s. The shaded curve indicates interannual variability in ENSO index (Nino 1+2), defined as the sea-surface temperature change over (0–10°S, 90°W–80°W) region in the Pacific Ocean (source: www.cpc.ncep.noaa.gov/data/indices). See color version of this figure at back of this issue.

[1999]. For the period 1993–1996, the inverse model values fail to show strong positive anomalies observed by *Feely et al.* [1999]. The causes for the underestimation are not clear, but presumably are due to the lack of atmospheric observations in the eastern equatorial Pacific. Since the ocean basis functions have spatially uniform flux distribution, atmospheric observations at different locations receive biased response from the changes in regional flux intensity.

[16] On the basis of the time series observations of multiple parameters at the BATS station near Bermuda Island (32°N, 64.3°W; station 12 in Figure 1), basin-scale CO_2 fluxes have been estimated by *Gruber et al.* [2002] for the North Atlantic (Figure 4b). The TDI model results are in good agreement with the observations until 1994, but following that opposite behavior is observed. The latter time period coincides with the time when CO_2 measurements at several locations were started in 1992/1993. This suggests that two Bermuda stations play a major role in constraining the fluxes from North Atlantic region. Flux patterns within an inverse model region depend on the area of source-signal footprint of the point measurements. Thus as the number of observations increases within an inverse model region, correlations between the TDI flux anomaly and the results obtained from station measurements may be reduced depending on the spatial heterogeneity in the CO_2 flux distribution.

[17] As shown in Figure 4c, the amplitudes and phases of flux anomalies estimated on the basis of the surface water chemistry measurements at ALOHA Station (22.75°N, 158°W) [*Dore et al.*, 2003] are in fairly good match alternatively with our results for the southern and northern North Pacific (NP) areas. Since the atmospheric CO_2 observations at this location are likely to be influenced by both the northern and southern North Pacific air masses, such behavior is explicable. During the positive PDO phase the wind stress is westerly over the central Pacific and northerly along the eastern Pacific [*Mantua et al.*, 1997], thus the CO_2 flux anomaly of NP(S) for the period 1996–1998 matches well with the ALOHA observations. For the negative PDO phase in 1999–2001 the flux anomaly of NP(N) captures most of the CO_2 variability observed at ALOHA station. On the basis of the 1988–2002 time series observations of CO_2, ^{13}C and salinity, *Keeling et al.* [2004] concluded that the observed change of this area from a CO_2 sink to a weak source is due mainly to an increased transport of higher salinity waters from the north, perhaps associated with a regime shift in PDO around 1997. Their findings are consistent with our results.

3.6. Sea-Air CO_2 Flux Anomalies and Climate Variability

[18] Large-scale recursive patterns of climate anomalies such as ENSO and the NAO account for a large part of climate variability on interannual to sub-decadal timescales [*Hurrell*, 1995; *Trenberth et al.*, 1998]. Climate mode shifts are associated with changes in temperature distributions and

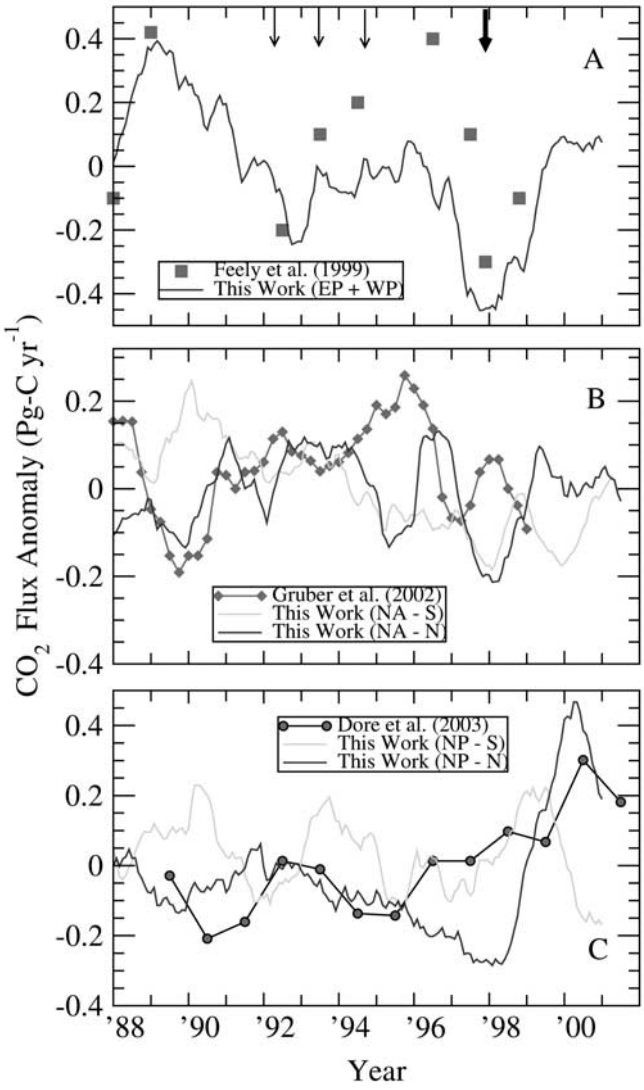

Figure 4. Variations in TDI flux anomalies from (a) Tropical Pacific, (b) North Atlantic, and (c) the North Pacific regions are shown in comparison with previous estimations based on oceanic and atmospheric observations. An average seasonal cycle is subtracted from the monthly mean TDI fluxes to calculate the flux anomalies for each inverse model region. The 12-month running means are shown in Figure 4b, while 24-month running means are taken for the rest to reduce the noise (high frequency variability). The arrows in Figure 4a indicate the onset of El Niño events; while the one started in 1992 was prolonged and that during 1997/1998 was more pronounced. The actual emission rates at ALOHA (supplied by John Dore) are converted to area integrated flux anomalies for the whole NP region (area $\sim 50 \times 10^{12}$ m^2) (Figure 4c). See color version of this figure at back of this issue.

large-scale circulations of the ocean and the atmosphere, and they, in turn, would affect sea-air CO_2 fluxes through changes in physical and biological processes in upper oceans. Many of the prominent climate modes are regional and have particular domains of influence. In what follows, we shall examine the relationship between regional sea-air CO_2 flux anomalies and climate variations using a correlation analysis. In particular, we focus on anomalous climatic conditions represented by ENSO, the NAO and PDO. The choice of these climate modes is by no means exhaustive, but their domains of influence collectively cover a large part of the global ocean. The variability of sea-air CO_2 flux for six oceanic regions in the period 1988–2001 are shown in Figure 5 and compared with the three major climate indices.

[19] In our analysis, we emphasize the fact that those climate modes have particular peak seasons. For the ENSO cycle, El Niño matures during an early part of the boreal winter, and hence the ENSO-related variations in sea-surface temperatures and winds are pronounced during the months of December, January and February. Similarly, the NAO variability, associated with anomalous surface westerly winds over the North Atlantic, is concentrated in boreal winter, for example, December through March. Also, the PDO represents the leading mode of sea-surface temperature variability over the North Pacific particularly for the period of November to March. In recognizing the periods, in which climate conditions are most affected, anomalies of CO_2 flux and climate indices averaged over the period of three different peak periods are used for the analysis (Table 3): December to February (DJF) for ENSO, December to March (D to M) for the NAO, and November to March (N to M) for the PDO. These average values are collectively referred to as "winter" values. We then examine correlations between the winter mean climate indices and monthly CO_2 flux anomalies averaged over the winter months.

[20] As noted above, large-scale climate modes may have delayed effects on sea-air CO_2 fluxes owing to slow responses of marine ecosystems and other environments. In order to take into account these effects, we also examine lagged relationships between the "winter" climate indices and monthly averaged CO_2 flux anomalies using a simple lagged cross-correlation analysis, which is referred hereafter to as lagged correlations. In Table 3, the lag time is expressed in the number of months that CO_2 flux anomalies lag behind the winter climate indices, starting from January (+1) to December (+12).

[21] For all correlations calculated in this study, we employ the same significance test with the null hypothesis that there is no correlation between a climate index and CO_2 flux anomaly. Since there is no prior knowledge about the sign of correlations, we use the two-sided t-test. This is in contrast to an alternative null hypothesis that a correlation between a climate index and CO_2 flux anomaly is non-negative or -positive, which leads to a one-sided t-test. An autocorrelation analysis reveals a sharp drop in the autocorrelation functions of all climate indices used in this study with 1 year of lag. On the basis of this result we use the same sample size of 14 to estimate the critical values of $|r| = 0.52$ and 0.65 for the 95% and 99% significance levels, respectively. The null hypothesis is then rejected with 95 or 99% confidence if correlation coefficient (r) exceeds these values.

3.6.1. El Niño–Southern Oscillation

[22] ENSO is a climate mode that manifests ocean-atmosphere coupled processes in the tropical Pacific. During its

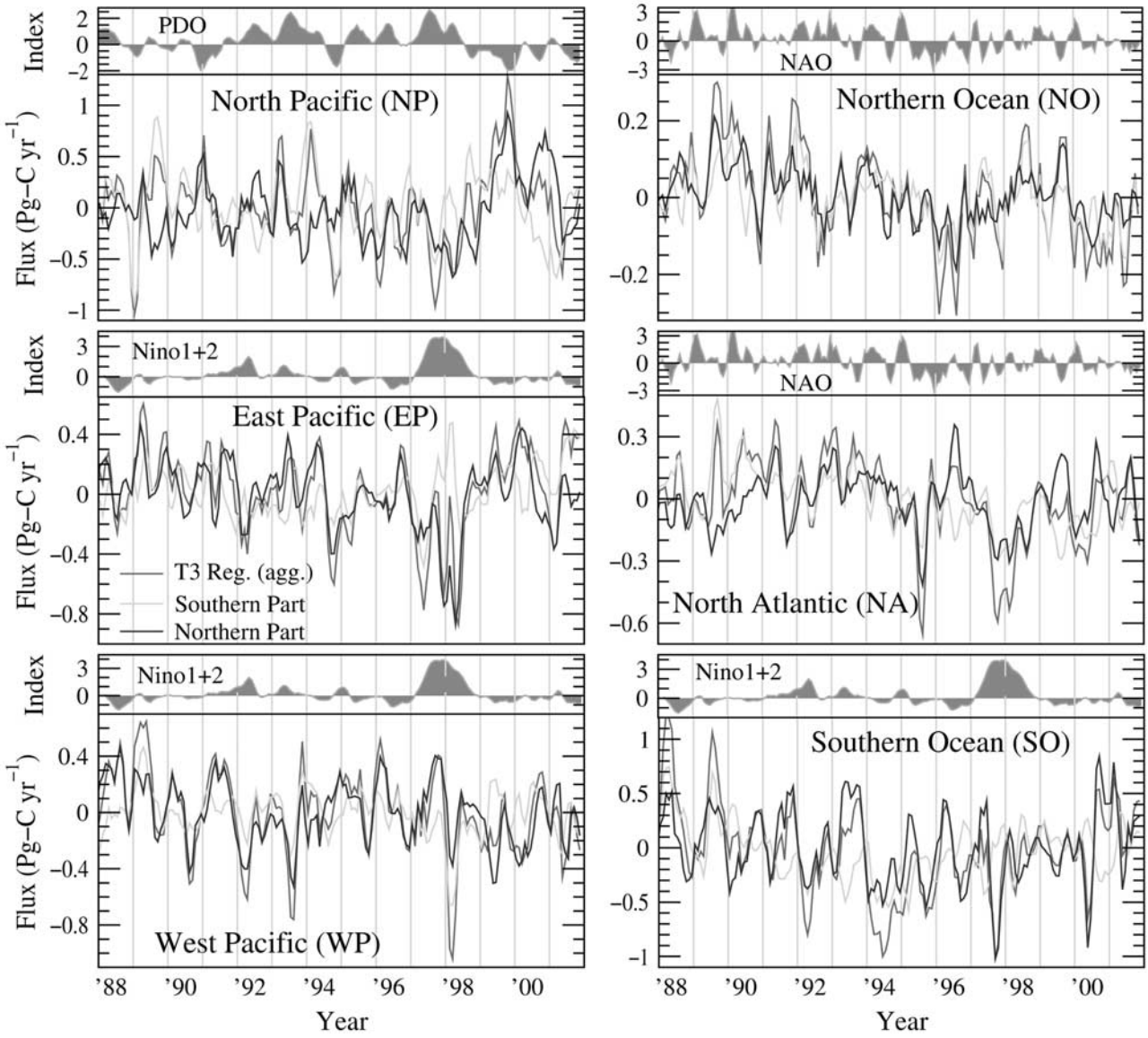

Figure 5. Flux anomalies (green line: south part, blue line: north part, red line: aggregated to TransCom-3 region size) are shown for selected ocean regions, where physical changes are observed by the known decadal climate variability, and the flux uncertainty reductions are greater than 20% (except two NO regions, which have low prior uncertainties) by inversion. The flux anomalies are calculated by subtracting the long-term mean seasonal cycle from monthly mean fluxes for each region. The related climate oscillation indices are shown in the top part of each panel. Three-monthly running means are taken for all the data. Note that CO_2 flux data are treated differently for calculating the correlation coefficients (see text). The following data sources are used for the climate indices: www.cpc.ncep.noaa.gov for ENSO, www.cru.uea.ac.uk for NAO, and tao.atmos.washington.edu for PDO. See color version of this figure at back of this issue.

warm phase, El Niño, the surface water over the eastern half of the tropical Pacific becomes anomalously warm with weakened trade winds. The opposite conditions prevail during the cold phase, La Niña. Although the center of ENSO action is located in the tropical Pacific, its climatic influence extends to a large area outside of the tropical Pacific through both oceanic and atmospheric dynamical connections [*Trenberth et al.*, 1998]. Some indices for ENSO are based on sea-surface temperatures (SSTs), while others are based on atmospheric sea level pressure (SLP). In this analysis, we use the Nino1+2 index, which is defined as SST anomalies averaged over the region of 0°–10°S and 80°W–90°W. This area is located off the coast of Peru, where CO_2 fluxes are sensitively affected by the intensity of upwelling and hence by El Nino events. Thus this index is a sensitive indicator for the ENSO events.

Table 3. Correlation Coefficients Between CO_2 Flux Anomalies and Climate Indices for 22 Ocean Regions Based on the Results From the Control Run[a]

Region	Nino1+2		NAO		PDO	
Name	DJF	Lagged	D to M	Lagged	N to M	Lagged
NP(N)	−0.30	−0.58(+3)	−0.00	...	−0.54	−0.66(+5)
NP(S)	0.06	−0.58(+5)	0.10	...	0.30	...
WP(N)	0.16	...	−0.16	−0.55(+9)	0.16	...
WP(S)	−0.63	−0.74(+1)	0.25	...	−0.28	−0.60(+1)
EP(N)	−0.74	−0.74(+4)	0.39	...	−0.50	−0.52(+2)
EP(S)	0.44	0.77(+2)	−0.15	...	−0.16	−0.71(+7)
SP(N)	0.28	0.73(+9)	−0.15	...	−0.07	0.52(+6)
SP(S)	−0.30	−0.67(+5)	0.18	0.71(+4)	0.23	−0.64(+5)
NO(N)	0.18	...	0.71	0.53(+3)	−0.01	...
NO(S)	0.11	0.79(+8)	0.73	0.65(+1)	−0.13	...
NA(N)	−0.39	−0.55(+3)	0.14	−0.72(+7)	−0.03	...
NA(S)	−0.45	−0.52(+2)	0.13	0.59(+11)	−0.17	...
TA(N)	−0.27	...	0.32	...	0.01	−0.53(+10)
TA(S)	−0.03	...	−0.14	0.56(+11)	−0.27	...
SA(N)	−0.52	−0.62(+1)	0.05	...	−0.30	−0.53(+1)
SA(S)	−0.34	...	0.27	...	−0.04	...
SO(N)	−0.00	...	−0.59	−0.55(+1)	−0.09	−0.62(+12)
SO(S)	0.06	...	0.11	−0.61(+11)	0.03	...
TI(N)	−0.06	−0.55(+4)	0.55	0.58(+2)	0.09	0.52(+6)
TI(S)	0.39	...	0.68	0.62(+1)	0.36	...
SI(N)	0.29	...	0.27	−0.52(+10)	0.19	0.57(+8)
SI(S)	−0.37	...	−0.18	−0.54(+10)	−0.58	−0.65(+1)

[a]The regions are organized for those in the Pacific, the Atlantic, and others from the top. As is described in the text, the sample size is 14 in all cases, representing the boreal winters of 1988 to 2001 for the winter averaged CO2 flux anomalies. Columns 2, 4, and 6 show winter correlations, while columns 3, 5, and 7 are lagged for correlations (for definitions, see section 3.6). For winter correlations, those exceeding the critical value of [0.52] for the 95% significance level are in boldface. For lagged correlations, only those with the maximum or minimum correlations exceeding the >95% significance level are shown with lag time in parentheses. Three dots indicate that there is no significant lagged correlation for a particular region.

[23] Column 2 in Table 3 shows correlation coefficients for the DJF mean CO_2 fluxes versus DJF mean Nino1+2 index. Significant levels of correlation are found between the CO_2 flux and the Nino1+2 index for WP(S) ($r = -0.63$) and EP(N) ($r = -0.74$), whereas all other areas in the Pacific do not show significant levels of correlation. The negative correlations observed in these two equatorial areas indicate that the colder SST correlates with positive CO_2 flux anomalies. This is consistent with the observations that the eastern equatorial Pacific is a strong CO_2 source during the cold phase (La Niña events). When time lag is taken into account, correlations between the winter Nino1+2 indices and monthly CO_2 fluxes are greatly improved (see column 3 in Table 3, where the lag time in months is indicated in the parentheses). Significant correlations (with $|r| > 0.58$) are found in nearly all parts of the North and South Pacific with the exception of the northwestern tropical Pacific area, WP(N). The signs of the correlation coefficients are negative in all areas but two equatorial areas, EP(S) and SP(N). This finding supports the notion that warmer SSTs during El Niño lead to reductions in upwelling of CO_2-rich deep waters, thereby reducing the magnitude of sea-to-air CO_2 fluxes.

[24] Some puzzling features are found for the computed CO_2 flux values. As shown in Table 3 and Figure 5 (green curve in the middle left panel), CO_2 flux anomalies are estimated positive (i.e., increased sea-to-air flux) for the eastern tropical South Pacific, EP(S), area during the 1997/1998 El Niño event. On the contrary, observations show that the sea-to-air CO_2 flux is suppressed during the strong El Niño event by the influx of warm low-CO_2 surface waters from the west. But atmospheric CO_2 observations are totally lacking in the EP(S) area (see Figure 1). Thus we consider that a dipole feature between the EP(N) and EP(S) areas during the 1997/1998 El Niño period is attributable to the lack of observational constraints and likely to be an artifact. Since these areas are a major oceanic CO_2 source and are affected strongly by the El Niño–La Niña events, atmospheric CO_2 observations are urgently needed.

[25] A significant positive lagged correlation is found for the temperate South Pacific, SP(N) ($r = 0.73$ with +9 month lag time; see Figure 6a). Our CO_2 flux estimate for this area is constrained by observations at stations 25 and 58 in Figure 1. Both stations are located within the extratropical horseshoe-shaped region, in which positive SST anomalies are observed during the cold phase of ENSO, when sea-to-air fluxes are large owing to enhanced upwelling near South America. This accounts for the positive correlation obtained for this area. The observed positive lagged correlation for SP(N) may be attributable to a successive occurrence of the 1997/1998 El Niño followed closely by the 1999/2000 La Niña event.

[26] The tropical western North Pacific region, WP(N), shows no significant correlation either with or without lag (columns 2 and 3, Table 3). On the other hand, its southern counterpart, WP(S), has a strong negative correlation coefficient ($r = -0.74$ with +1 month lag time). Since both of these regions are constrained in the western and eastern ends by the shipboard measurements (stations 47–58 in Figure 1) of atmospheric CO_2 and the high altitude aircraft observations (stations 79–86 in Figure 1), this north-south contrast appears to be real. Oceanographic observations indicate that sea surface temperature and pCO_2 in the equatorial warm pool areas (5°N–5°S, west of the date line) are not sensitive to El Niño conditions [*Takahashi et al.*, 2003]. Therefore the difference in correlation coefficients between the northern and southern areas may be attributed to the oceanographic conditions outside the equatorial belt. In the western tropical Pacific, the ocean water circulation pathways in the Northern Hemisphere are different from those in the Southern Hemisphere. The WP(N) area (0°–15°N) receives waters from the North Equatorial Current and Equatorial Countercurrent as well as the South Equatorial Current, whereas the WP(S) area (0°–15°S) receive mostly the South Equatorial Current water. These features are reflected in the observed north-south asymmetrical distribution of chlorophyll in tropical and temperate surface waters of the Pacific [*Gregg and Conkright*, 2002]. On the basis of temperature analysis in upper 400 m of the North Pacific, *Schneider et al.* [1999] concluded that there is no significant coupling between the northern midlatitude Pacific and the equatorial region via advection along the thermocline. Such oceanographic features may account for the North-South asymmetry of the correlation coefficients in the tropical western Pacific. However, no simple explana-

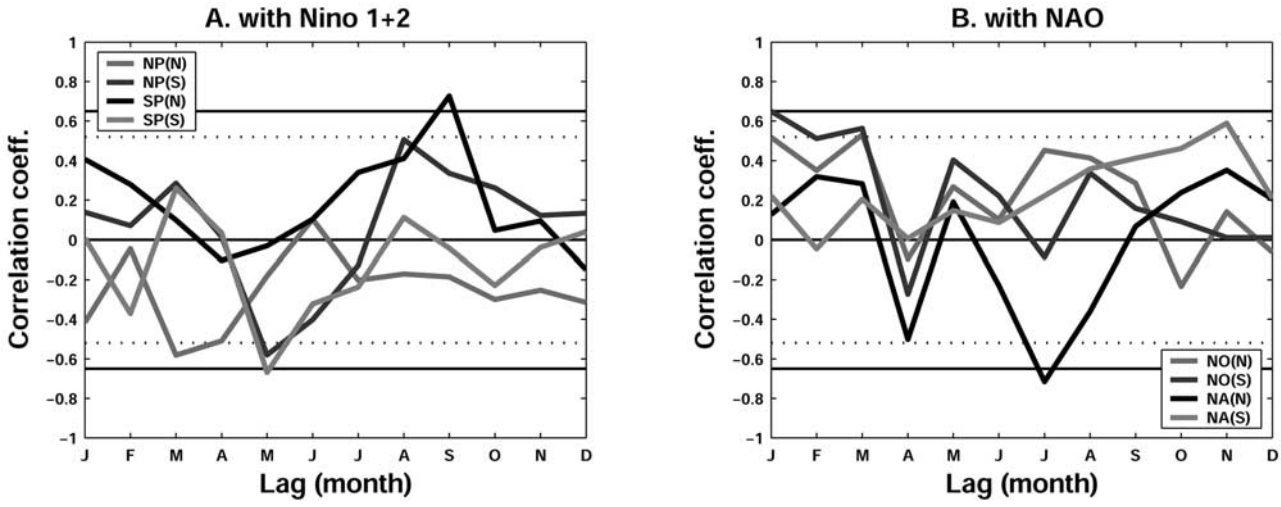

Figure 6. Lagged cross-correlations of the winter mean climate indices with monthly CO_2 flux anomalies: (a) for the Nino1+2 index over the extratropical Pacific region and (b) for the NAO index over the North Atlantic region. Individual sub-regions are described in the legend. Lag starts from January and ends in December. The 95% and 99% significance levels are indicated by broken and solid lines, respectively. See color version of this figure at back of this issue.

tion can be offered to account for the north-south asymmetry in the correlation coefficients in this region.

[27] The areas with significant correlations are not limited within the Pacific basin. We find a significant correlation with time lag for the subarctic and temperate North Atlantic, NO(S), NA(N) and NA(S), as well as in the temperate South Atlantic, SA(N) ($r = -0.62$ with +1 month time lag). A total of 5 areas out of 14 in the Atlantic, Indian and Southern oceans have significant correlations with various lag times. Of these five areas, only the subarctic Atlantic, NO(S), has positive correlation and the remaining four areas in the Atlantic and tropical Indian Ocean, TI(N), show negative correlations. A general picture that emerges from this analysis is that the CO_2 fluxes over the global oceans tend to decrease during the warm phase of ENSO.

[28] The above analysis based on the Nino1+2 index provides only a partial picture of the relationship between CO_2 flux anomalies and ENSO, and other ENSO indices may capture different aspects of CO_2 flux-ENSO relationships. In order to examine this possibility, we have repeated the same correlation analysis using the Nino3.4 index that gives a stronger focus on the central tropical Pacific. The results are largely consistent with those based on the Nino1+2 index. Similarly, being aware of sampling biases due to the extremeness of 1997/1998 El Niño, we have repeated the above analysis on the basis of the non-parametric Spearman's rank correlation method. Despite some differences, the overall picture remains unchanged.

3.6.2. North Atlantic Oscillation

[29] The NAO index represents variability in surface westerly winds over the North Atlantic, which affect temperature distributions and other climatic conditions over the Euro-Atlantic sector and a large part of the Eurasian continent. Our analysis is based on the NAO index defined as the difference in normalized December–March mean SLP between Lisbon and Stykkisholmur, Iceland [*Hurrell*, 1995]. The positive phase of the NAO is associated with enhanced surface westerlies over the North Atlantic, a deeper than average Icelandic low, and a weaker than average Azores high. The NAO has its activities centered in the Atlantic and is uncorrelated with ENSO on interannual timescales. For example, the correlation between the Nino1+2 and NAO indices over the study period is 0.06. Hence the inclusion of the NAO index to our correlation analysis would provide additional information on the relationships between regional CO_2 flux anomalies and climate variability. As seen in Table 3 (column 4), the winter mean CO_2 flux anomalies show negligible correlation with the winter mean NAO index in the Pacific basin. In comparison, the CO_2 flux anomalies of the Northern Ocean areas, NO(N) and NO(S), are correlated with the NAO index significantly with $r = 0.71$ or better for the winter mean values. In fact, the NAO accounts for about one half the interannual variance of the estimated winter-averaged CO_2 flux anomalies of this region ($r^2 \sim 0.5$). The positive polarity of the NAO is associated with stronger storm activities and vertical mixing in the North Atlantic sub-polar gyre region, NO(S). They bring CO_2-rich deeper waters to the surface, thereby enhancing the mid-winter sea-to-air CO_2 flux and increasing the CO_2 uptake flux in spring. Figure 6b shows the variations of correlation coefficients with different lag times for the North Atlantic. For NO(S), it shows positive correlations ($r = 0.51$ to 0.65) consistently over the period of January through March, which coincides with the months of strong North Atlantic storm activities. This is followed by a sharp reversal in April. A similar pattern is seen for NO(N) and NA(N) though in different magnitudes. These sign reversals appear to indicate the influence of spring blooms in the sub-polar region. The above results are consistent

with the observations that CO_2 flux anomalies in sub-polar regions are largely controlled by two factors, winter upwelling of sub-surface waters and plankton blooms in spring [*Takahashi et al.*, 2002].

[30] Another feature notable in Table 3 is significant seasonal correlations for the Southern Ocean, SO(N), and the tropical Indian Ocean, TI(S) and TI(N). Studies based on climate model simulations suggest that part of the recent NAO trend toward its positive polarity is attributed to warm conditions in the tropical Indian Ocean [*Hoerling et al.*, 2001; *Hurrell et al.*, 2004]. Their results may imply a climate connection between the North Atlantic and the Indian Ocean. However, the timescale of their analyses is longer compared to monthly or interannual timescales considered in this study. Thus the question of the sources of significant seasonal and monthly lagged correlations for the Indian Ocean remains open.

3.6.3. Pacific Decadal Oscillation

[31] The PDO is defined as the leading principal component of North Pacific monthly SST anomalies (poleward of 20°N) [*Mantua et al.*, 1997]. It represents basin-scale decadal climate variability that highlights a SST dipole pattern between the central North Pacific and the northern coastal region off the North American continent. A regression analysis of sea level pressure on the PDO index shows that it is strongly related to anomalous atmospheric circulation associated with the variation in the Aleutian low. The PDO appears to covary with ENSO on interannual timescales: the correlation coefficient of the Nino1+2 and PDO indices is 0.45 (90% significant level). Thus, for our short analysis period of 14 years, we regard the PDO as representing interannual variability in SST, in particular the part associated with the above SST dipole, which is closely related to ENSO through the Aleutian low variability.

[32] The mean winter PDO index for the northern North Pacific area, NP(N), shows a significant negative correlation with $r = -0.54$ (Column 6 Table 3). The positive phase of the PDO is associated with negative SST anomalies and more vigorous winter mixing over the central North Pacific. In addition, during the positive phase of the PDO, wind directions off Canada tend to be northward thus suppressing the upwelling of high CO_2 waters from depth [*Mantua et al.*, 1997]. The negative seasonal correlation seems to indicate, on seasonal timescales, the importance of coastal upwelling among all processes. A significant negative lagged correlation in May ($r = -0.66$ with +5 months lag; column 7) in this area further suggests the importance of the delayed effects from enhanced productivity, whereas other significant lagged correlations in the Pacific sector seem attributable to co-variability with the ENSO cycle judging from a comparison with the correlations with ENSO, for example, SP(S).

[33] The southern South Indian Ocean, SI(S), shows significant negative correlation ($r = -0.58$) between the CO_2 flux anomalies and the boreal winter mean index (column 6). We also found some significant lagged correlations (column 7) in the Indian sector, TI(N), SI(N) and SI(S). Although the CO_2 flux anomalies in the Indian Ocean areas exhibit significant lagged correlation values for Nino1+2, NAO and PDO, their climatological implications are not clear.

4. Conclusions

[34] The net sea-air CO_2 fluxes from 22 ocean regions (and 42 land regions) have been estimated for the period 1988–2001 using a time-dependent inverse model and atmospheric CO_2 concentrations observed at 87 stations around the globe. The case studies suggest that the derived CO_2 flux anomalies are robust against the changes in the initial conditions (flux and data uncertainties) used in the inverse model calculation.

[35] The long-term mean CO_2 uptake over the globe is estimated to be in the range of 1.05–1.40 Pg-C yr^{-1} for the land and 1.58–2.02 Pg-C yr^{-1} for the ocean during 1990–2000. These estimates are consistent with the results based on the changes observed in the concentrations of atmospheric CO_2 and oxygen. Our results are also consistent broadly with the time-space distribution of CO_2 fluxes that have been estimated on the basis of ocean time series measurements. On the other hand, we found that the sea-air CO_2 flux values obtained by various investigators using the inversion of atmospheric CO_2 concentration data differ significantly from one another. Such differences may be attributed to the selection of observational data and region partitioning in inverse models.

[36] The estimated CO_2 flux anomalies are distinct from region to region. A correlation analysis was conducted to examine the relationships of CO_2 flux anomalies with three major climate modes, ENSO, the PDO, the NAO. Since these climate modes manifest themselves prominently during certain peak seasons, mean climate indices for the boreal "winter" months have been used to compute correlation with the "winter" mean sea-air CO_2 flux anomalies. In addition, lagged correlations have been examined using the monthly mean CO_2 flux anomaly. Our regional sea-air CO_2 flux values are correlated with climate indices at >95% significant levels in many parts of the global oceans. The sea-air CO_2 flux anomalies correlate significantly with the Nino1+2 index over the entire Pacific as well as over the subarctic and temperate North Atlantic Ocean. The flux anomalies over the north and tropical Atlantic correlate significantly with the NAO index. The Indian and Southern Ocean CO_2 flux anomalies also correlate significantly with the NAO index. The flux anomalies over the Pacific and some areas of the Indian and Southern Oceans appear to correlate with the PDO index. Possible oceanographic significance of these correlations has been discussed.

[37] We recognize that the CO_2 fluxes in some areas such as the eastern tropical Pacific Ocean are poorly constrained owing to the lack of atmospheric CO_2 measurements. For example, the sea-to-air CO_2 flux values obtained in this study for the southeastern tropical Pacific, EP(S), increase during the 1997/1998 El Nino. This is contrary to the oceanographic observations and is likely attributed to the absence of the atmospheric observations. Accordingly, some of the correlations found in this study may be artifacts, although many of them appear to be robust. We believe that our implementation of a 64-region inverse model has helped

to improve our understanding of the effects of climate variations on sea-air CO_2 fluxes at regional to global spatial scales.

[38] **Acknowledgments.** This work has benefited from several talks during 3rd TransCom-3 meeting at Max-Planck-Institute, Jena, in May 2003. We thank R. Law (also for the comments), K. Gurney, and P. J. Rayner for making the TDI model code available to us. The comments from Nicolas Gruber on an earlier version of this manuscript are greatly appreciated. T. T. has been supported by a NASA grant (NAG5-11357). Advice offered by Douglas Martinson of LDEO on statistical analysis is gratefully acknowledged. Earth Simulator and SX-5 computer systems have been used extensively for making the forward and inverse model simulations, respectively. We thank both the anonymous reviewers for helpful comments.

References

Aumont, O., J. C. Orr, P. Monfray, W. Ludwig, P. Amiotte-Suchet, and J.-L. Probst (2001), Riverine-driven interhemispheric transport of carbon, *Global Biogeochem. Cycles*, *15*(2), 393–406.

Battle, M., M. L. Bender, P. P. Tans, J. W. C. White, J. T. Ellis, T. Conway, and R. J. Francey (2000), Global carbon sinks and their variability inferred from atmospheric CO_2 and $\delta^{13}C$, *Science*, *287*, 2467–2470.

Bousquet, P., P. Peylin, P. Ciais, C. L. Quere, P. Friedlingstein, and P. Tans (2000), Regional changes in carbon dioxide fluxes of land and ocean since 1980, *Science*, *290*, 1342–1346.

Dore, J. E., R. Lukas, D. W. Sadler, and D. M. Karl (2003), Climate-driven changes to the atmospheric CO_2 sink in the subtropical North Pacific Ocean, *Nature*, *424*, 754–757.

Feely, R. A., R. Wanninkhof, T. Takahashi, and P. Tans (1999), Influence of El Niño on the equatorial Pacific contribution of atmospheric CO_2 accumulation, *Nature*, *398*, 597–601.

Francey, R. J., P. Tans, C. E. Allison, I. G. Enting, J. W. C. White, and M. Trolier (1995), Changes in oceanic and carbon uptake since 1982, *Nature*, *373*, 326–330.

GLOBALVIEW-CO2 (2002), *Cooperative Atmospheric Data Integration Project: Carbon Dioxide* [CD-ROM], Natl. Oceanic and Atmos. Admin., Clim. Monit. and Diag. Lab., Boulder, Colo. (Available via anonymous FTP to ftp.cmdl.noaa.gov, path: ccg/CO2/GLOBALVIEW)

Gloor, M., N. Gruber, J. L. Sarmiento, C. L. Sabine, R. A. Feely, and C. Rödenbeck (2003), A first estimate of present and preindustrial air-sea CO_2 flux patterns based on ocean interior carbon measurements and models, *Geophys. Res. Lett.*, *30*(1), 1010, doi:10.1029/2002GL015594.

Gregg, W. W., and M. E. Conkright (2002), Decadal changes in global ocean chlorophyll, *Geophys. Res. Lett.*, *29*(15), 1730, doi:10.1029/2002GL014689.

Gruber, N., C. D. Keeling, and N. R. Bates (2002), Interannual variability in the North Atlantic Ocean carbon sink, *Science*, *298*, 2374–2378.

Gurney, K. R., R. M. Law, P. J. Rayner, and A. S. Denning (2000), TransCom-3 experimental protocol, *Pap. 707*, Dep. of Atmos. Sci., Colo. State Univ., Fort Collins.

Gurney, K. R., R. M. Law, A. S. Denning, P. J. Rayner, B. Pak, and the TransCom-3 L2 modelers (2004), Transcom-3 Inversion Intercomparison: Control results for the estimation of seasonal carbon sources and sinks, *Global Biogeochem. Cycles*, *18*, GB1010, doi:10.1029/2003GB002111.

Hoerling, M. P., J. W. Hurrell, and T. Xu (2001), Tropical origins for recent North Atlantic climate change, *Science*, *292*, 90–92.

Hurrell, J. W. (1995), Decadal trends in the North Atlantic Oscillation regional temperatures and precipitation, *Science*, *269*, 676–679.

Hurrell, J. W., M. P. Hoerling, A. S. Phillips, and T. Xu (2004), Twentieth century North Atlantic climate change: Part 1. Assessing determinism, *Clim. Dyn.*, *23*, 371–389.

Keeling, C. D., T. P. Whorf, M. Wahlen, and J. van der Plicht (1995), Interannual extremes in the rate of rise of atmospheric carbon dioxide since 1980, *Nature*, *375*, 666–670.

Keeling, C. D., et al. (2001), Exchanges of atmospheric CO_2 and $\delta^{13}CO_2$ with the terrestrial biosphere and oceans from 1978 to 2001: I. Global aspects, *Ref. Ser. 01-06*, Scripps Inst. of Oceanogr., La Jolla, Calif.

Keeling, C. D., H. Brix, and N. Gruber (2004), Seasonal and long-term dynamics of the upper ocean carbon cycle at Station ALOHA near Hawaii, *Global Biogeochem. Cycles*, *18*, GB4006, doi:10.1029/2004GB002227.

Keeling, R. F., and H. E. Garcia (2002), The change in oceanic O_2 inventory associated with recent global warming, *Proc. Natl. Acad. Sci.*, *99*, 7848–7853.

Kistler, R., et al. (2001), The NCEP-NCAR 50-Year Reanalysis: Monthly means CD-ROM and documentation, *Bull. Am. Meteorol. Soc.*, *82*, 247–268.

Le Quéré, C., et al. (2003), Two decades of ocean CO_2 sink and variability, *Tellus, Ser. B*, *55*, 649–656.

Maksyutov, S., and G. Inoue (2000), Vertical profiles of radon and CO_2 simulated by the global atmospheric transport model, *CGER/NIES-I039-2000-7*, pp. 39–41, Cent. for Global Environ. Res., Ibaraki, Japan.

Mantua, M. J., S. R. Hare, Y. Zhang, J. M. Wallace, and R. C. Francis (1997), A Pacific interdecadal climate oscillation with impacts on salmon production, *Bull. Am. Meteorol. Soc.*, *78*, 1069–1079.

Marland, G., T. A. Boden, and R. J. Andres (2003), Global, regional, and national fossil fuel CO_2 emissions, in *Trends: A Compendium of Data on Global Change*, Carbon Dioxide Inf. Anal. Cent., Oak Ridge Natl. Lab., Oak Ridge, Tenn.

McNeil, B. I., R. J. Matear, R. M. Key, J. L. Bullister, and J. L. Sarmiento (2003), Anthropogenic CO_2 uptake by the ocean based on the global chlorofluorocarbon data set, *Science*, *299*, 235–239.

Patra, P. K., M. Ishizawa, S. Maksyutov, T. Nakazawa, and G. Inoue (2005), Role of biomass burning and climate anomalies for land-atmosphere carbon fluxes based on inverse modeling of atmospheric CO_2, *Global Biogeochem. Cycles*, *19*, GB3005, doi:10.1029/2004GB002258.

Plattner, G.-K., F. Joos, and T. F. Stocker (2002), Revision of the global carbon budget due to changing air-sea oxygen fluxes, *Global Biogeochem. Cycles*, *16*(4), 1096, doi:10.1029/2001GB001746.

Prentice, I. C., et al. (2001), The carbon cycle and atmospheric carbon dioxide, in *Climate Change 2001: The Scientific Basis*, edited by J. T. Houghton et al., chap. 3, pp. 183–237, Cambridge Univ. Press, New York.

Rayner, P. J., I. G. Enting, R. J. Francey, and R. Langenfelds (1999), Reconstructing the recent carbon cycle from atmospheric CO_2, $\delta^{13}C$ and O_2/N_2 observations, *Tellus, Ser. B*, *51*, 213–232.

Rödenbeck, C., S. Houweling, M. Gloor, and M. Heimann (2003), CO_2 flux history 1982–2001 inferred from atmospheric data using a global inversion of atmospheric transport, *Atmos. Chem. Phys.*, *3*, 1919–1964.

Sarmiento, J. L., P. Monfray, E. Maier-Reimer, O. Aumont, R. J. Murnane, and J. C. Orr (2000), Sea-air CO_2 fluxes and carbon transport: A comparison of three ocean general circulation models, *Global Biogeochem. Cycles*, *14*(4), 1267–1281.

Schneider, N., A. J. Miller, M. A. Alexander, and C. Deser (1999), Subduction of decadal north Pacific temperature anomalies: Observations and dynamics, *J. Phys. Oceanogr.*, *29*, 1056–1070.

Takahashi, T., et al. (2002), Global sea-air CO_2 flux based on climatological surface ocean pCO_2, and seasonal biological and temperature effects, *Deep Sea Res., Part II*, *49*, 1601–1622.

Takahashi, T., S. C. Sutherland, R. A. Feely, and C. Cosca (2003), Decadal variation of the surface water pCO_2 in the western and central equatorial Pacific, *Science*, *302*, 852–856.

Tans, P., I. Fung, and T. Takahashi (1990), Observational constraints on the global atmospheric CO_2 budget, *Science*, *247*, 1431–1438.

Trenberth, K. E., et al. (1998), Progress during TOGA in understanding of modeling global teleconnections associated with tropical sea surface temperatures, *J. Geophys. Res.*, *103*, 14,291–14,324.

Wanninkhof, R. (1992), Relationship between wind speed and gas exchange, *J. Geophys. Res.*, *97*, 7373–7382.

Wanninkhof, R., and W. M. McGillis (1999), A cubic relationship between gas transfer and wind speed, *Geophys. Res. Lett.*, *26*, 1889–1892.

M. Ishizawa, S. Maksyutov, and P. K. Patra, Frontier Research Center for Global Change, Japan Agency for Marine-Earth Science and Technology, 3173-25 Showa-machi, Yokohama 236 0001, Japan. (Misha.Ishizawa@ec.gc.ca; shamil@nies.go.jp; prabir@jamstec.go.jp)

T. Nakazawa, Center for Atmospheric and Oceanic Studies, Graduate School of Science, Tohoku University, Sendai 980-8578, Japan. (nakazawa@mail.tains.tohoku.ac.jp)

T. Takahashi and J. Ukita, Lamont-Doherty Earth Observatory, Columbia University, PO Box 1000, RT 9W, Palisades, NY 10964-8000, USA. (taka@ldeo.columbia.edu; jukita@ldeo.columbia.edu)

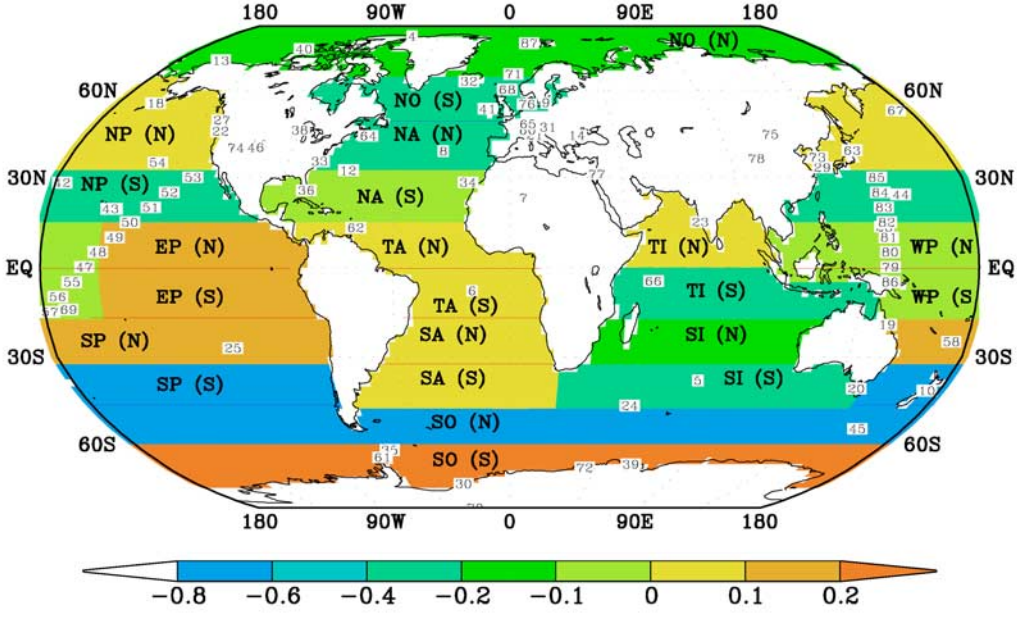

Figure 1. The 22 ocean regions in the TDI model (42 land regions, similar to those of *Patra et al.* [2005], are not shown here to avoid complexity) and the surface observation network (87 stations) used in this study. The long-term mean fluxes (except the 1997–1998 period) are indicated by the color of each region (see the color bar at the bottom of the figure). The negative and positive values indicate net uptake and net release by the ocean, respectively. Names of 11 ocean regions in TransCom-3 are as follows: 1, North Pacific (NP); 2, West Pacific (WP); 3, East Pacific (EP); 4, South Pacific (SP); 5, Northern Ocean (NP); 6, North Atlantic (NA); 7, Tropical Atlantic (TA); 8, South Atlantic (SA); 9, Southern Ocean (SO); 10, Tropical Indian (TI); and 11, South Indian (SI). These regions are divided into north (N) and south (S) parts in this work. Details of a priori and a posteriori flux uncertainties for the ocean regions are given in Table 2, and a glimpse of CO_2 concentrations and associated data uncertainties at each of the 87 stations are available in Table S1 in the auxiliary material.

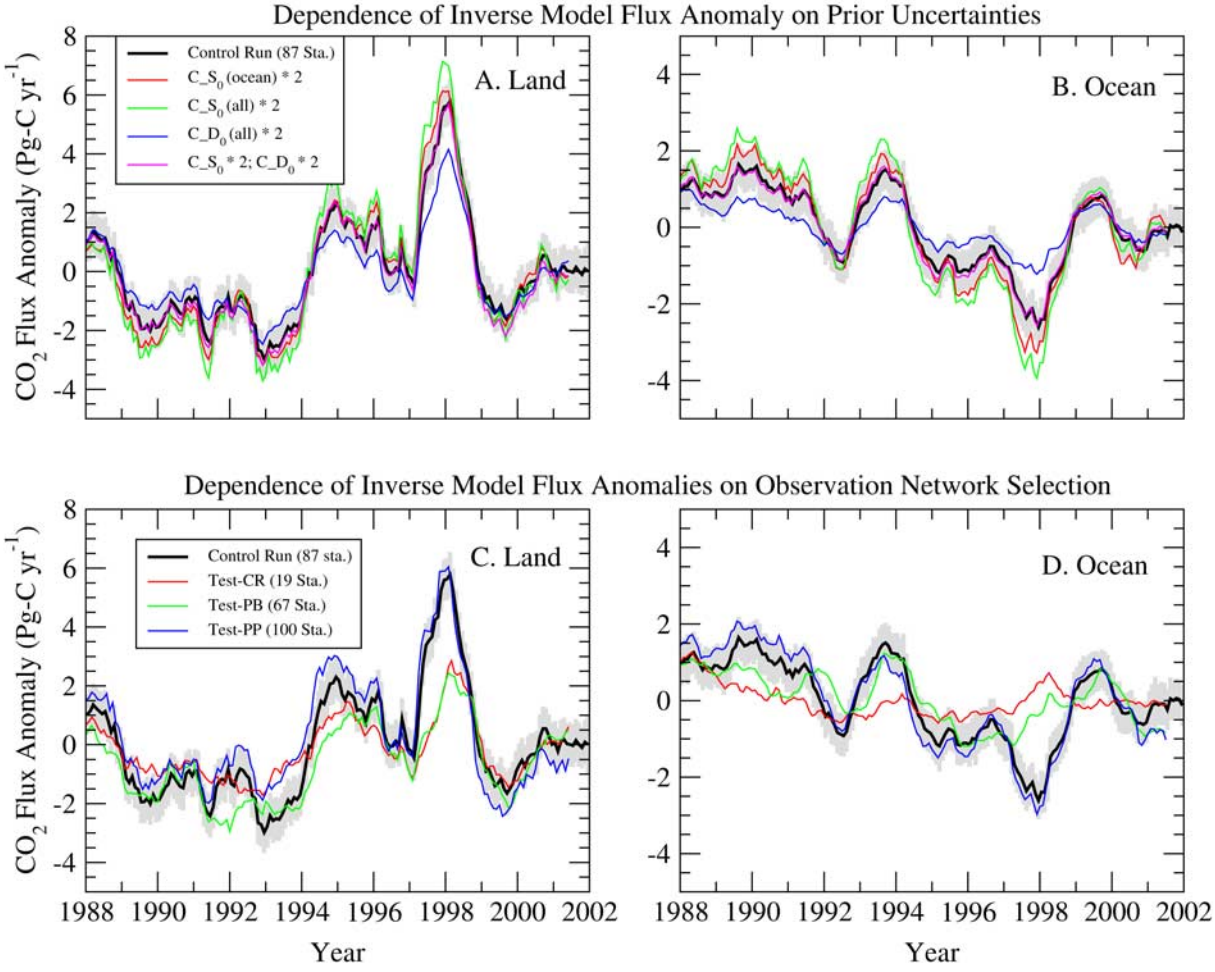

Figure 2. CO_2 flux anomalies as estimated by TDI calculation for total land and ocean from atmospheric CO_2 data, with varying network sizes as well as different a priori data and source uncertainties. Flux anomaly is calculated by subtracting an average seasonal cycle for the period 1988–2001 from the monthly-mean CO_2 fluxes. The cases shown in Figures 2a and 2b are obtained by (1) control run (thick black line), (2) ocean $C_{S0} \times 2$, (3) all $C_{S0} \times 2$, (4) $C_{D0} \times 2$, and (5) all $C_{S0} \times 2$ and $C_{D0} \times 2$. The cases shown in Figures 2c and 2d are obtained by (1) control run, and different CO_2 data networks, (2) Test-CR, (3) Test-PB, and (4) Test-PP. The a posteriori flux estimate uncertainties obtained from control TDI model run are shown as the grey shading. The tick marks indicate January of the corresponding years.

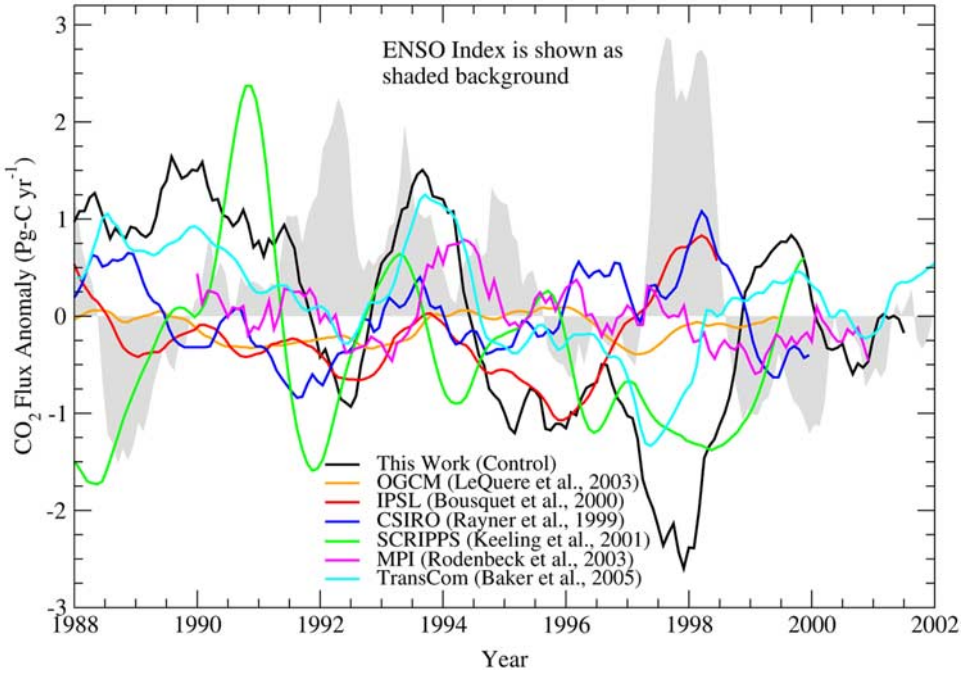

Figure 3. Global ocean flux anomalies (deseasonalized) estimated by different groups using inverse models, ocean models, and carbon isotope deconvolution techniques. The description of OGCM, CSIRO, and SCRIPPS models can be found in details elsewhere [*Le Quéré et al.*, 2003, and references therein]. The results from *Rödenbeck et al.* [2003] are due to an observation network of 19 stations, which is selected to show the flux variability for the 1990s. The shaded curve indicates interannual variability in ENSO index (Nino 1+2), defined as the sea-surface temperature change over (0–10°S, 90°W–80°W) region in the Pacific Ocean (source: www.cpc.ncep.noaa.gov/data/indices).

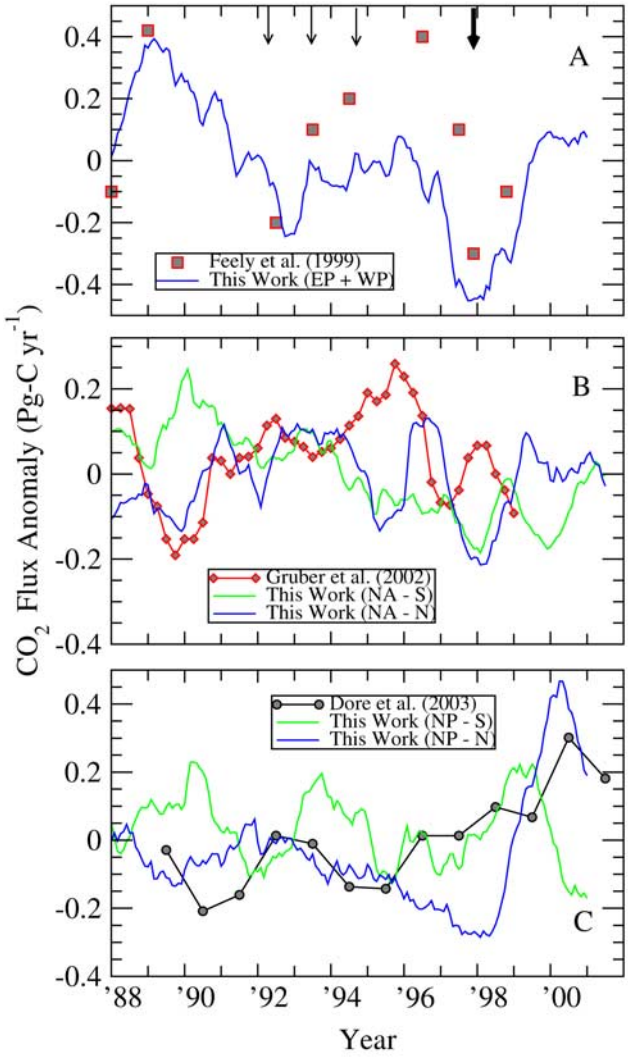

Figure 4. Variations in TDI flux anomalies from (a) Tropical Pacific, (b) North Atlantic, and (c) the North Pacific regions are shown in comparison with previous estimations based on oceanic and atmospheric observations. An average seasonal cycle is subtracted from the monthly mean TDI fluxes to calculate the flux anomalies for each inverse model region. The 12-month running means are shown in Figure 4b, while 24-month running means are taken for the rest to reduce the noise (high frequency variability). The arrows in Figure 4a indicate the onset of El Niño events; while the one started in 1992 was prolonged and that during 1997/1998 was more pronounced. The actual emission rates at ALOHA (supplied by John Dore) are converted to area integrated flux anomalies for the whole NP region (area $\sim 50 \times 10^{12}$ m^2) (Figure 4c).

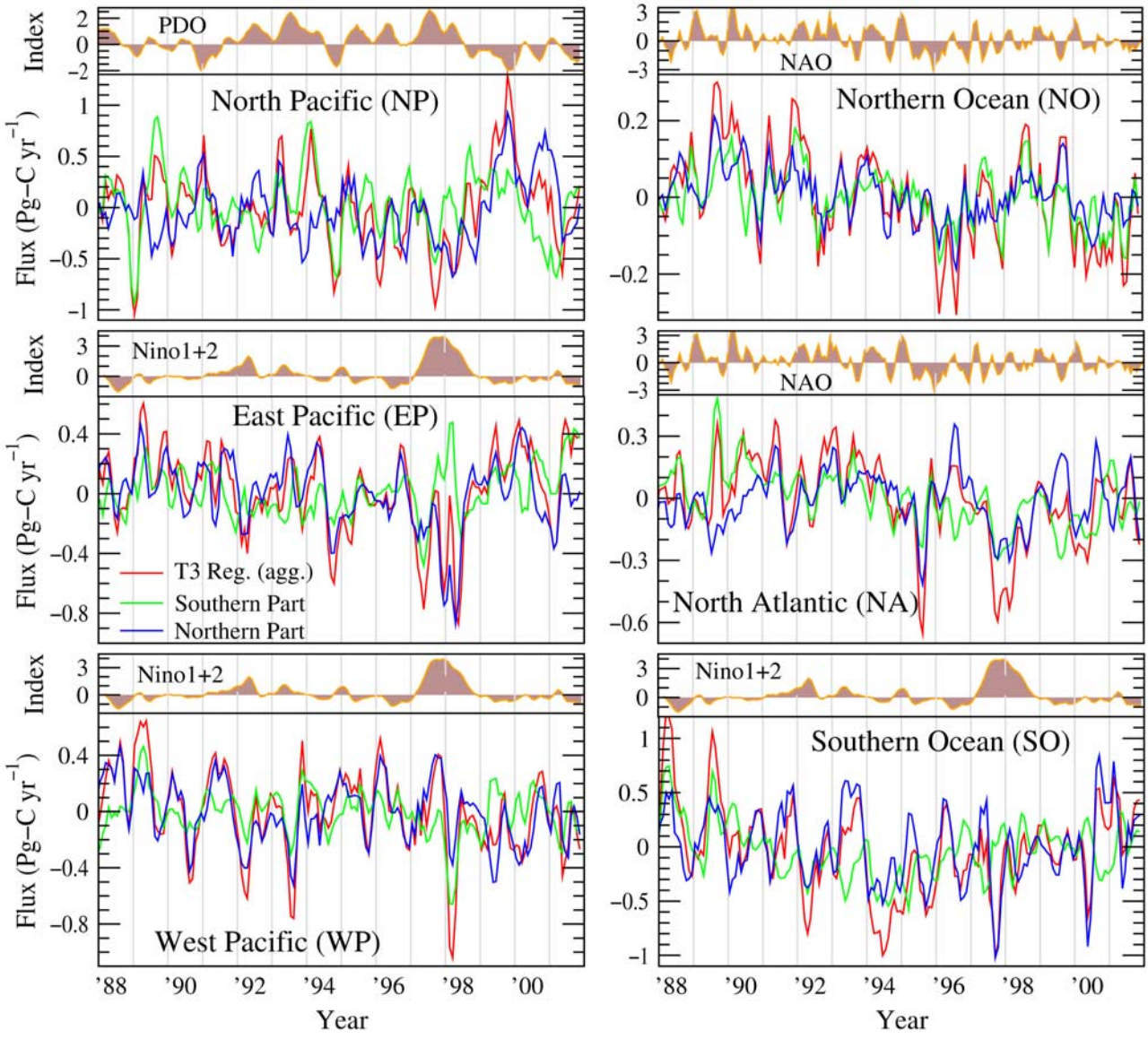

Figure 5. Flux anomalies (green line: south part, blue line: north part, red line: aggregated to TransCom-3 region size) are shown for selected ocean regions, where physical changes are observed by the known decadal climate variability, and the flux uncertainty reductions are greater than 20% (except two NO regions, which have low prior uncertainties) by inversion. The flux anomalies are calculated by subtracting the long-term mean seasonal cycle from monthly mean fluxes for each region. The related climate oscillation indices are shown in the top part of each panel. Three-monthly running means are taken for all the data. Note that CO_2 flux data are treated differently for calculating the correlation coefficients (see text). The following data sources are used for the climate indices: www.cpc.ncep.noaa.gov for ENSO, www.cru.uea.ac.uk for NAO, and tao.atmos.washington.edu for PDO.

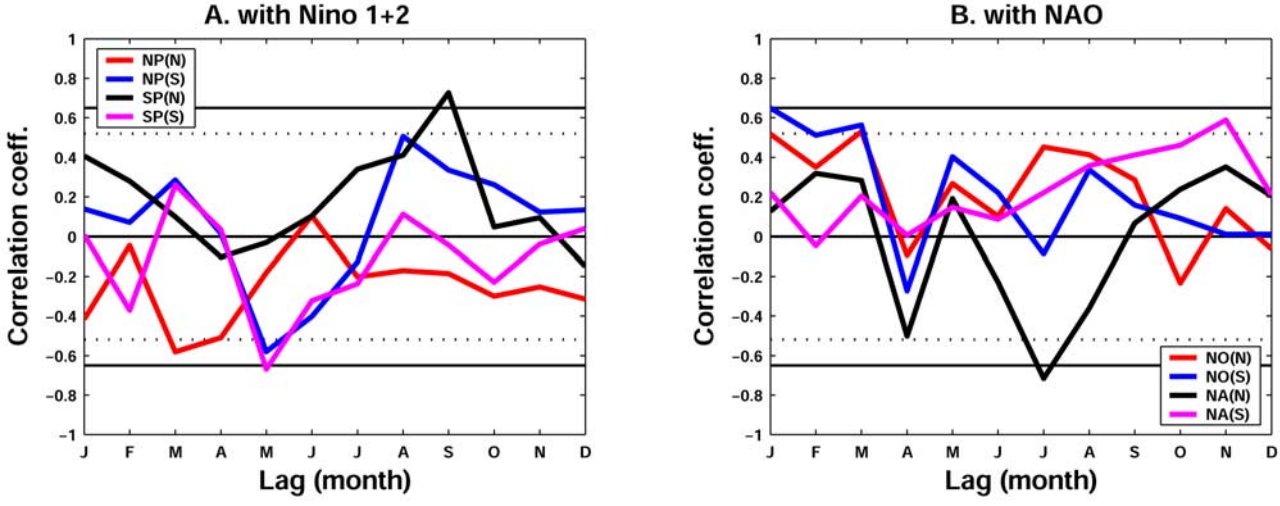

Figure 6. Lagged cross-correlations of the winter mean climate indices with monthly CO_2 flux anomalies: (a) for the Nino1+2 index over the extratropical Pacific region and (b) for the NAO index over the North Atlantic region. Individual sub-regions are described in the legend. Lag starts from January and ends in December. The 95% and 99% significance levels are indicated by broken and solid lines, respectively.